Passive Synthetic Aperture Radar Imaging Using Radio-Astronomical Sources

Sean T. Peters, *Member, IEEE*, Dustin M. Schroeder, *Senior Member, IEEE*,
Mark S. Haynes, *Member, IEEE*, Davide Castelletti, *Member, IEEE*, and Andrew Romero-Wolf

Abstract—Recent work has demonstrated a passive radio sounding approach that uses the Sun as a source for echo detection and ranging. As the Sun is a moving source with a position that is known *a priori*, we evaluate this technique's capabilities to measure the echo's phase history, map topography, and perform synthetic aperture radar (SAR) focusing. Here, we present our approach to implementing passive SAR using a compact, temporally incoherent radio-astronomical source as a signal of opportunity. We first evaluate the passive system's capabilities to obtain an echo from a rough surface by determining the critical signal-to-noise ratio (SNR) for reliably observing the Sun's echo reflection with our passive instrument. We then demonstrate that our technique can detect the necessary changes in range, phase, and reflectivity of an echo from the Sun. We next present the experimental results of our passive radar testing using the Sun at Dante's View, Death Valley, to highlight this technique's ability to perform 2-D imaging. Finally, with synthetic data, we demonstrate that we can use time-domain backprojection to focus a planar white noise signal, perform passive SAR imaging, and improve the measurement's SNR and azimuth resolution. The results of passive SAR focusing on white noise highlight the potential for the Sun and Jupiter's radio emissions to perform surface and subsurface imaging for planetary and terrestrial observations.

Index Terms—Passive radar, passive radio sounding, passive synthetic aperture radar (SAR), radio echo sounding.

I. INTRODUCTION

PASSIVE radars have shown great promise as a low-resource remote sensing approach by using ambient radio signals of opportunity, such as Global Positioning System (GPS) [1], Digital Video Broadcasting-Terrestrial (DVB-T) [2], and radio-astronomical emissions [3]–[6], instead of transmitting a signal for echo detection as done by active systems. Such passive implementations of remote sensing would be desirable for radio glaciological monitoring at large spatial scales, where radio-echo sounding is the principal technique for monitoring ice sheet thickness and subsurface

conditions, both terrestrially [7], [8] and on the icy moons of Jupiter [9], [10].

The appeal of a passive radar that exploits signals of opportunity for radioglaciological measurements become even more apparent when considering the size, power, cost, and logistical demands of repeat active radar surveys. As active radar systems must transmit their own powerful electromagnetic signal for detection, any attempts to perform repeat measurements on airborne platforms [11] or ground-based surveys [12] require significant logistical or financial overhead that often limits such repeats to seasonal or yearly campaigns [13]. Since glaciers evolve over time-spans ranging from years [14], [15] to months [16], and even weeks [17] to days [18], current active radar surveys are unable to capture these processes at this desired span of temporal resolutions across a continent-sized scale. Passive radio sounding would thus serve as a low-resource approach to provide a wide range of temporal and spatial observations of glaciers, ice sheets, and ice shelves by using ambient radio emissions instead of transmitting their own signals [6].

Nevertheless, further improvements to passive radar sounding are required for such an implementation, as the user no longer has control over the radar signal's waveform, power, source location, nor transmission event [2]. Consequently, the passive system's incomplete knowledge and control of the externally transmitted signal results in reduced signal-to-noise ratio (SNR) and degraded resolution when compared to an active radar [2]. Furthermore, the polar regions have few well-defined man-made radio sources that have the ideal center frequency, spectral characteristics, and power levels necessary for a practical passive ice-penetrating radar. Our passive sounding development has therefore focused on using wideband radio-astronomical sources, such as the Sun and Jupiter, as signals of opportunity to perform radioglaciological observations [6].

While using the Sun's radio waves for remote sensing introduces several challenges [6], it is available half the year in even the most remote of polar regions, its elevation and azimuth positions are well known, and its spatial coherence and white-noise characteristics produce distinct echo peaks in the autocorrelation function [6]. The passive approach works by receiving the direct path of the astronomical noise source and then recording long enough to obtain the reflected path from the ice-subsurface interface [3]–[6]. By correlating the direct emission with the reflected signal, one can extract the white noise echo's amplitude and delay time; this delay time

between the direct and reflected echo peaks in the correlation then maps to an ice thickness estimate. We previously demonstrated passive radio sounding using the Sun as a signal for echo detection [6], [19], [20]. We now look to improve the performance of passive radar using radio-astronomical sources by using synthetic aperture radar (SAR) techniques.

SAR focusing is a well-known signal processing technique for remote sensing, as it allows radar systems on moving platforms to create a narrow virtual beamwidth; this long synthetic aperture is then used to perform surface and subsurface imaging with a finer azimuth resolution [21]. As SAR processing also improves the measurement's SNR [22]–[26], this technique is also desirable for passive radar sounding to increase the range of possible glaciological coverage, including temperate glaciers that have high attenuation losses. To perform SAR processing, backprojection is an attractive focusing algorithm [27]–[33], and the one that we will explore for this analysis, as it avoids the geometric approximations and assumptions that break down for other techniques (such as the Range-Doppler algorithm, $\omega - k$ algorithm, and the Chirp Scaling algorithm) in the limits of large imaging size, wide bandwidths, and high-resolution imaging at lower frequencies [34], [35]; however, backprojection is more computationally expensive [28].

Previous work has studied passive SAR focusing of coherent, digital, man-made signals of opportunity by modifying these focusing algorithms [36]–[39] and, more recently, using deep learning to reconstruct the SAR image [40]; however, there has been little work to date that has examined whether one can use a temporally incoherent white-noise signal for passive SAR focusing, such as the Sun. As previous passive sounding work has concentrated on using radio-astronomical signals, such as Jupiter's decametric radiation and the Sun's radio emissions, to perform radar sounding of Europa's icy shell [3]–[5] and terrestrially [6], we examine these sources' potential for passive SAR focusing.

The focus of this article is to present an implementation of passive radar designed for radio-echo sounding and SAR focusing using a compact white noise source (i.e., the Sun and Jupiter's radio emissions). The technical barriers for such an approach include extracting the amplitude and delay time of an echo from a rough surface, as well as tracking the changes in range, phase, and reflectivity of the Sun's echo in the autocorrelation function. In addition to demonstrating our approach's ability to overcoming these challenges, we evaluate the system's performance requirements, probability of detection metrics, and the critical SNR for passive sounding. We ultimately seek to monitor ice sheets with an SNR and resolution that is comparable to an active radar by using a system that can perform passive SAR using the Sun. A passive receiver could then map the topography of the ice sheet bed by tracking the Sun and its reflection point as the Sun moves throughout the entire day. If the instrument were deployed for long periods of time, this measured range profile would allow one to monitor ice-shelf melt rates [41], or even reflectivity changes as the Sun's trace crosses a subglacial drainage path or ice shelf channel [42]. This system would operate with much lower power consumption because it has no transmitter. Also,

by storing the final coherently summed autocorrelated result, the data-volume and data-rate would be much lower than an active radar [6]. At a minimum, this demonstration serves as an additional step to developing a low-resource passive radar that uses the Sun's radio signals for continuous monitoring of glaciers, ice sheets, and ice shelves at a continental scale.

Our article is organized as follows. In Section II, we discuss the theoretical background of passive sounding and SAR focusing in the context of receiving a white noise signal. In Section III, we present the proposed signal processing techniques and developed hardware system used in the passive radio sounding experiments. In Section IV, we present our experimental results obtained from the Death Valley field experiment, where the goal is to measure changes in the range, reflectivity, and phase of the received white noise signal. We expand on this by demonstrating passive SAR focusing with a compact radio-astronomical white-noise signal with synthetic data. Finally, we summarize the results of our passive SAR study in Section VI and conclude by discussing the applications and key follow-on questions for passive SAR using astronomical signals in a radioglaciological context.

II. THEORETICAL BACKGROUND

We briefly derive the radar equations for the passive and active sounding cases, starting from the fluxes of the signal and taking into account the backscatter for a flat Fresnel zone; we then use these equations to calculate the relative passive SNR for the direct and reflected signals. We conclude this section with an overview of passive SAR focusing and describe our white noise focusing approach using backprojection.

A. Passive Sounding Radar Equation

For passive sounding with radio-astronomical sources, we assume that the distant source arrives as a plane wave. Due to this plane wave nature, the same plane wave that is received by the instrument is also incident on the target and then reflects back to the instrument. Letting the power density of the incident field as it passes the instrument be S, the received power of the direct signal, P_d, and the reflected signal, P_r, are, respectively, [43]

$$P_d = \frac{SG_d\lambda^2}{4\pi} \tag{1}$$

$$P_r = \frac{SG_r\lambda^2\sigma}{(4\pi)^2 R^2} \tag{2}$$

where G_d is the gain of the antenna in the direction of the source, G_r is the gain of the receiver's antenna in the direction of the target, λ is the wavelength, R is the distance to the target, and σ is the target backscatter.

We note that this equation is for an arbitrary target and will be used to compute the scattered power of facets in the passive SAR simulator that we describe in Section IV-C. We then consider the expression for a radar backscatter cross section, σ, of a flat, coherent dielectric disk at normal incidence [44]

$$\sigma = \Gamma \frac{4\pi A^2}{\lambda^2} \tag{3}$$

where Γ is the surface reflectivity, and A is the area of the disk. The target area for the Fresnel zone is $A = \pi r_f^2 = \pi((\lambda h)^{1/2})^2$, where $r_{f,p} = (\lambda h)^{1/2}$ is the Fresnel zone radius for passive sounding at nadir [5], [43] and h is the platform height. Substituting this into the passive radar equation, the received power becomes [43]

$$P_r = \Gamma \frac{S G_r \lambda^2 \pi}{4}. \tag{4}$$

Therefore, for a flat Fresnel zone that increases linearly with altitude, there is no range dependence by virtue of the incident plane wave. This shows that the passive signal does not experience geometric spreading loss for flat Fresnel zone targets, which is consistent with [3], [5].

Furthermore, dividing the received direct and reflected power by the receiver noise, the SNRs of the direct and reflected signals are

$$SNR_d = \frac{P_d}{k T_n B_r} \tag{5}$$

$$SNR_r = \frac{P_r}{k T_n B_r} \tag{6}$$

where k is the Boltzmann's constant, T_n is the noise temperature, and B_r is the receiver bandwidth. In general, the power ratio of the reflected signal to the direct signal is

$$\frac{P_r}{P_d} = \frac{S G_r \lambda^2 \sigma}{(4\pi)^2 R^2} \frac{4\pi}{S G_d \lambda^2} = \frac{G_r}{G_d} \frac{\sigma}{4\pi R^2}. \tag{7}$$

We note that 7 is the ideal case where direct signal leakage is not considered; moreover, Equations 1 and 2 are used to construct the signals that fully describe the case where leakage from the direct and reflected signals are taken into account for the Passive SAR simulations (32 and 33, Section IV-C). The power ratio of 32 and 33 should therefore be used when including the leakage signals.

Using again the target area equal to the Fresnel zone, $\sigma = \Gamma 4\pi^3 R^2$, the power ratio becomes

$$\frac{P_r}{P_d} = \frac{G_r}{G_d} \Gamma \pi^2 \tag{8}$$

which is independent of the target distance. However, if the altitude is high enough that the Fresnel zone follows the curvature of the planetary body, R_c, then at altitudes $h \gg R_c$, the passive received power obtains $1/R^2$ losses, which is discussed in detail in [3].

B. Active Sounding Radar Equation

To form a basis of comparison for the passive radar equation, we provide the active radar equation, which is used widely in terrestrial and planetary radio glaciology [9], [10], [44] for investigating icy subsurface conditions. The traditional radar equation [45] for the received power is

$$P_r = \frac{P_t G_t G_r \lambda^2 \sigma}{(4\pi)^3 R^4}. \tag{9}$$

Substituting the expression for a radar cross section of a flat, coherent dielectric disk (3), where $r_{f,a} = (\lambda h/2)^{1/2}$ is the

Fresnel zone radius for active sounding at nadir, the active radar equation becomes [43], [44]

$$P_r = \Gamma \frac{P_t G_t G_r \lambda^2}{2^6 R^2}. \tag{10}$$

Both active radar equations 9 and 10 have geometric spreading losses even for a flat Fresnel zone, whereas the passive radar equation (4) experiences no geometric spreading loss in that case.

C. Passive SAR Theory

Here, we adapt and extend passive SAR focusing to include astronomical sources, which are distant sources with radiation that arrive as plane waves. Previous passive SAR focusing techniques modify the active SAR focusing algorithms by either taking into account the timing and geometric uncertainties of the source's transmission event and location [36]–[39] or using deep learning models to invert and reconstruct the passive SAR image [40]. However, these methods assume coherent, digital, man-made sources. Starting from the acquisition geometry and the passive delay curves, we derive the constraint on the maximum integration time to focus the phase history of a white noise plane wave. We also derive the time-domain backprojection focusing algorithm for this signal.

1) Acquisition Geometry: In the classic SAR case, a radar system on a platform moves with velocity v and uses the Doppler information to focus the signal, as shown in Fig. 1. In the active case, the transmitter and receiver both move with velocity v. However, in the passive case, 1) a stationary receiver can listen to a moving source with a reflection point of velocity, v_s, 2) a moving receiver of velocity v can listen to a stationary source, or 3) both the receiver and the source can move.

We first consider a stationary receiver that records the moving source to image the reflective surface or subsurface. By the reciprocity relation of transmitting and receiving a signal with an antenna of gain, G_r, this setup allows passive SAR focusing even while the receiver is stationary. For typical values of λ and range, R, the maximum unfocused processing gain for a stationary receiver with a moving source is dictated by the Fresnel zone's $(\lambda R)^{1/2}$ relationship (i.e., the minor axis of an ellipse for off-nadir geometry) [43]. The maximum integration time due to the amount of time that the source's moving reflection point of velocity, v_s, is inside the diameter of the receiver's Fresnel zone is

$$T_{\max, f} = \frac{D_p}{v_s} = \frac{2\sqrt{\lambda R}}{v_s}. \tag{11}$$

2) Passive Delay Curves From a Moving Receiver: Now, we consider the case where both the receiver and the source can move as in Fig. 1. To estimate the ability of the passive radar to focus a white noise signal using the autocorrelation-based technique, we calculate delay curves corresponding to a surface point and observe the correlated pattern projected on the surface. The resulting time-delay curves will allow us to focus on the reflected radio emission. This is a first step to understanding the ability to discriminate between scattering points on the surface.
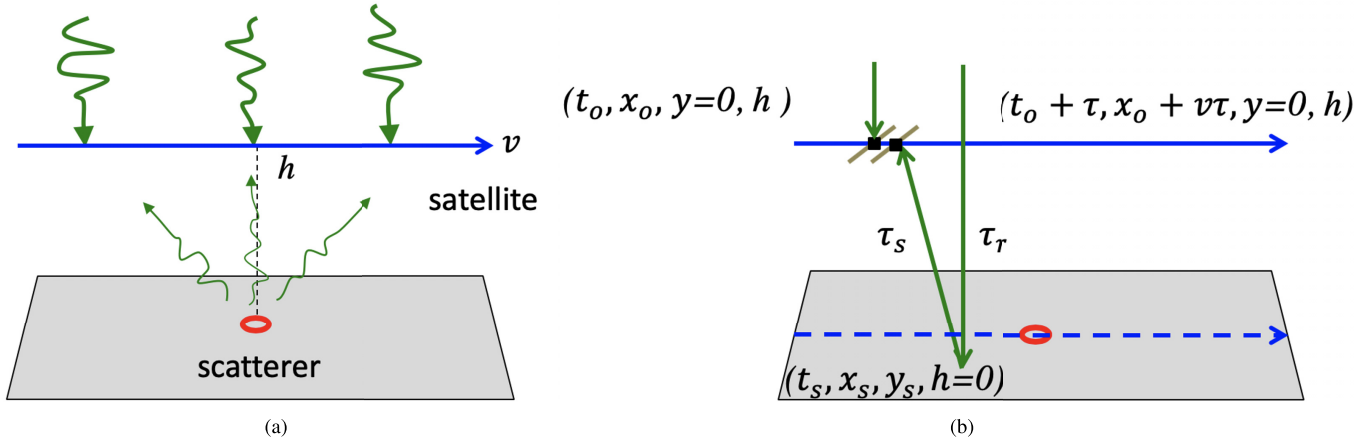
Fig. 1. Passive SAR concept. (a) The incoming signal and its scattered signal off the surface are measured by a receiver onboard a satellite platform of altitude h and velocity v. (b) As the platform moves, the receiver measures the direct path of the plane wave and its reflection off the surface.

We first define a reference time t_0 for the spacecraft position (t_0, x_0, h) with surface points of interest, x_s, and y_s as in Fig. 1. We then calculate the delay curve for a spacecraft of velocity, v, as a function of time, t.

From Fig. 1, the total delay time is $\tau = \tau_r + \tau_s$, where $\tau_r = (h/c)$ is the light propagation time from the parallel reference plane to the surface point, and the light propagation time from the surface point to the receiver point (assuming $v \ll c$) is

$$\tau_s = \frac{1}{c}\sqrt{(x - x_s)^2 + y_s^2 + h^2}. \tag{12}$$

This gives the delay equation

$$\tau(t|x_s, y_s, h, x_0, t_0) = \frac{1}{c}\left(h + \sqrt{(x(t) - x_s)^2 + y_s^2 + h^2}\right) \tag{13}$$

where $x(t) = x_0 + v(t - t_0)$ describes the spacecraft's position as a function of time.

3) Phase Focusing: Additionally, from standard SAR theory, the phase of the signal changes with a change in range. SAR theory relies on sampling the phase history to focus the signal which we show here.

The passive system records the direct white noise signal, $w(t)$, and the reflected signal with losses ρ

$$s(t) = w(t) + \rho w(t - \tau)e^{(-j2\pi r(t)/\lambda)} + n(t) \tag{14}$$

where from (13), the two-way range as a function of time is

$$r(t) = h + \sqrt{(x(t) - x_s)^2 + y_s^2 + h^2}. \tag{15}$$

Furthermore, the phase is a function of range

$$\phi_D(t) = \frac{2\pi}{\lambda}r(t) \tag{16}$$

and the change in phase over time is therefore

$$\lim_{t\to\infty}\frac{\partial\phi_D}{\partial t} = \frac{2\pi v}{\lambda}. \tag{17}$$

The change in phase as a function of velocity and wavelength requires that the autocorrelation is computed within an integration time interval of ΔT_{int} seconds to sample the phase history. The Doppler wave envelope can be deconvolved provided that the change in range is less than $\lambda/4$, which is the maximum allowable phase change assuming the system is heading directly at the object. As $t \to \infty$ in 17, this gives the following phase change

$$\Delta\phi_D(t) = \frac{\partial\phi_D}{\partial t}\Delta T_{\text{int}} \le \frac{\pi}{2}. \tag{18}$$

Therefore, no aliasing of the sampled phase occurs provided that the autocorrelation integration time intervals satisfy

$$\Delta T_{\text{int}} \le \frac{\lambda}{4v}. \tag{19}$$

Moreover, an integration time of $T_{\text{max},D} = \lambda/(4v)$ allows the receiver to sample the Doppler bandwidth and recover the phase history with the maximum time-bandwidth coherent processing gain. The passive radar's pulse repetition frequency (PRF) therefore must be greater than $4v/\lambda$ to compute the autocorrelation and perform phase focusing with the maximum integration time of $T_{\text{max},D}$. We note that in the case of passive sounding, where the noise signal exists continuously without time modulation, the PRF refers to the frequency at which individual passive measurements are received using an integration time of ΔT_{int} seconds, where in general, the PRF $\le 1/\Delta T_{\text{int}}$.

D. Performance Analysis: Active Versus Passive SNR After SAR Focusing

Using the derived integration time intervals, the time-bandwidth coherent processing gain from range compression is given by

$$G_{tb} = B_r \cdot \Delta T_{\text{int}} \tag{20}$$

where again B_r is the receiver bandwidth.

The azimuth processing gain is determined by the PRF of the receiver [46] as it receives for the duration that the signal's reflection point is inside the synthetic aperture, $T_{\text{max},ap}$.

Combining the maximum integration time with the PRF of the radar thus gives the azimuth processing gain

$$G_{az} = \text{PRF} \cdot T_{\text{max},ap}. \tag{21}$$

The SNR equation after range compression and azimuth processing is

$$\text{SNR}_r = \frac{P_r}{kT_nB_r} \cdot G_{tb} \cdot G_{az} \tag{22}$$

and after substituting in 20 and 21 for the range and azimuth processing gains becomes

$$\text{SNR}_{p,\text{SAR}} = \frac{P_r}{kT_nB_r}(B_r\,\Delta T_{\text{int}})\big(\text{PRF} \cdot T_{\text{max},ap}\big). \tag{23}$$

The general form of the passive SNR equation after SAR processing thus takes into account the receiver bandwidth (B_r), the integration time (ΔT_{int}), the PRF, and the total receiving time within the synthetic aperture ($T_{\text{max},ap}$), all of which are system design parameters. We note in particular that the length of $T_{\text{max},ap}$ can be limited by 1) the Fresnel zone in the case of a flat, coherent reflector [44], 2) the length of the radar's receive window when focusing onto a single isotropic scatterer [47], or 3) the surface's scattering function, which describes the regions in between these two extremes.

In the case of treating $T_{\text{max},ap}$ as the maximum amount of time that the moving reflection point is inside the antenna's aperture, and using the maximum integration time that still allows the receiver to sample the Doppler bandwidth as in 19, the SNR equation becomes

$$\text{SNR}_r = \frac{P_r}{kT_n}\frac{\lambda}{4v}\left(\text{PRF} \cdot \frac{\lambda h}{lv}\right). \tag{24}$$

Finally, in the case of the minimum possible PRF of $\text{PRF} = 4v/\lambda$, i.e., a 100% receiving duty cycle, the SNR equation for passive SAR becomes

$$\text{SNR}_r = \frac{P_r}{kT_n} \cdot \frac{\lambda h}{lv}. \tag{25}$$

The SNR equations for the active case are similar; however, the pulselength, τ_a, is used for the match filtering time-bandwidth gain instead of the integration time, ΔT_{int}. Additionally, while the azimuth processing gain, G_{az}, is of the same form as that of the passive case, the PRF for the active radar is typically much greater than for a passive radar that must record for duration $\Delta T_{\text{int}} \gg \tau_a$.

E. SAR Focusing With Time-Domain Backprojection

We provide an overview of our implementation of SAR focusing via time-domain backprojection. The expected result of focusing via backprojection is an increase in azimuth resolution and SNR as well as mapping the terrain of the illuminated surface.

The timing problem for acquiring the incoming noise has been previously discussed in [48], where the recorded incoming signal is cross-correlated with its backscattered fields. Here, we focus on the backprojection phase for an active and passive radar, as well as for off-nadir passive radar acquisitions. Fig. 2 shows the plane wave acquisition and backprojection geometry for active and passive radar cases.
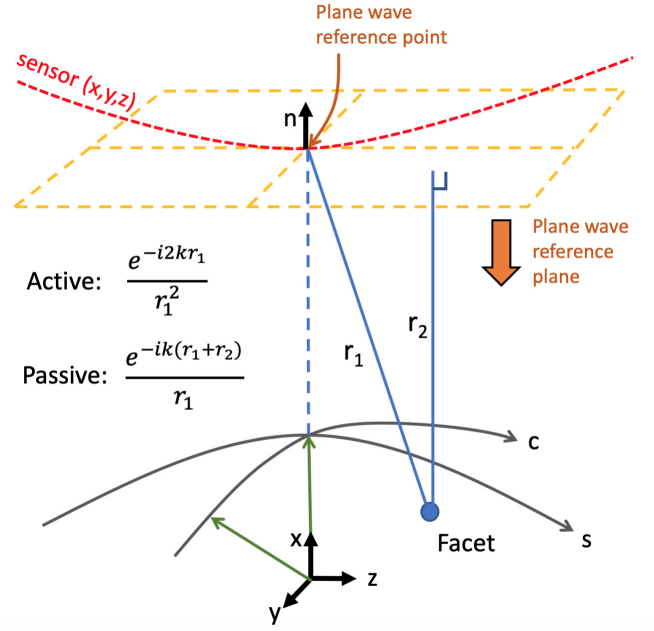

Fig. 2. Backprojection using plane-wave reference plane. While the slant range (one-way range delay) for active sounding is $\rho = r_1$, the slant range for passive sounding is $\rho = (r_1 + r_2)/2$.

1) Active Case: We use the backprojection algorithm as in [30]–[32]. The algorithm requires knowledge of the sensor geometry, altitude, and positions relative to the surface to then focus the reflectors within an aperture to the imaged, backprojected signal.

The received signal is first range-compressed with its respective reference signal, i.e., cross-correlated in the case of the passive system

$$C(t, u) = s(t, u) * s_o^*(-t) \tag{26}$$

where $s(t, u)$ is the incoming, received signal in fast-time, t, and slow-time, u, and $s_o(t)$ is the corresponding, reference signal (i.e., a plane wave in the passive case). The discrete fast-time samples of $C(t, u)$ are then interpolated to recover the correct range distances from the range-compressed data, where

$$t_{ij}(u) = \frac{2\sqrt{x_i^2 + (y_j - u)^2}}{c} \tag{27}$$

is the two-way travel time of the echoed signal for a target that is a distance r_1 away at position (x_i, y_j). Thus, each pixel has a time given by t_{ij} that is used to obtain the samples in the interpolated range-compressed data, $C[t_{ij}(u), u]$.

Next, for each pixel in the backprojected image, we select an illumination region in the range-compressed data that is the size of the synthetic aperture of length L. The imaging equation is therefore

$$f(x_i, y_j) = \sum_{u=-L/2}^{L/2} C[t_{ij}(u), u]e^{-i2\pi ft_{ij}(u)}. \tag{28}$$

In the active case, the target function formed via backprojection is thus multiplied by a phase function,

$e^{-i2kr_1} = e^{-i2\pi f t_{ij}(u)}$ in the range domain, where k is the angular wavenumber. In other words, each range compressed data point within an illuminated region is phase shifted by its corresponding path length distance, and then the contributions are summed over the aperture to focus the grid points to the image plane's pixels.

Thus, for a given synthetic aperture location, u, the fast-time data of $C(t, u)$ are backprojected to isolate the return of the reflector at (x_i, y_j). To summarize, the receive signal, $s(t, u)$, is first correlated by its reference signal, then the synthetic aperture region is interpolated and phase shifted by the corresponding range distance, and finally summed over an aperture to image that location as in 28.

2) Passive Case: Here, we describe the case for passively receiving the off-nadir plane wave, where we assume a timing situation that records the incoming signal with a sensor position that is relative to the plane-wave reference plane. While the slant range (one-way range delay) for active sounding is $\rho = r_1$, the slant range for passive sounding is $\rho = (r_1 + r_2)/2$, where r_2 is the perpendicular distance from a target to a plane that is perpendicular to the planar wave's direction and centered at the middle of the sensor line. The phase for the passive case is, therefore, $e^{-ik(r_1+r_2)}$, which is used in 28 to phase shift the fast-time data before summing over the synthetic aperture and focusing the signal via backprojection. This form of the backprojection equation and geometry in Fig. 2 is used for the Passive SAR simulations presented in Section IV-C.

III. METHODOLOGY

We present the developed hardware system and signal processing techniques used in the passive radar field testing at Dante's View, Death Valley, CA. In this experiment, the passive receiver remains stationary on the side of a cliff in Death Valley and tracks the Sun's moving reflection point of velocity, v_s, off the desert floor.

A. Hardware Components for Death Valley Experiments

The hardware that we use to record the Sun's direct path and desert floor reflection is similar to that described in our Passive Sea Cliff experiment, where our passive prototype used the Sun's radio waves to measure the height of a cliff [6]. The key hardware component is the Ettus E312 software-defined radio (SDR), which we use to digitize the Sun's radio frequency signal. The frontend of our receiver chain consists of a cavity-backed copper bowtie antenna that has 6.5 dBi of gain over 200–400 MHz and two cascaded Advanced Receiver low noise amplifiers (LNA). Each LNA provides 20 dB of gain with a 0.5 dB noise figure between 300 and 360 MHz.

B. System Configuration and Experiment Setup

We operate the SDR as a receiver with a 15.36 MHz bandwidth centered around 330 MHz. In the Death Valley environment, we determined this center frequency to minimize the amount of radio frequency interference (RFI) for our passive experiment; nevertheless, we remove any residual RFI

TABLE I
PASSIVE EXPERIMENT PARAMETERS

Description	Specification
Center Frequency	330 MHz
Instantaneous Bandwidth	15.36 MHz
Integration Time	8 seconds
Frontend Gain	104 dB
LNA Noise Figure	0.5 dB
Expected SNR	2.4 dB to 16.4 dB
Cliff Height	1780 meters
Fresnel Zone Radius	79.6 meters
Sun Angles	8 to 25 degrees

in postprocessing. Finally, the frequency spectrum centered at 330 MHz is free of man-made radio sources. Therefore, different from our Passive Sea Cliff experiment [6], we do not need to use notch filters to remove FM radio frequencies nor a low pass filter to avoid receiver saturation. The gain of the E312 SDR is set to 62 dB, which gives the receiver its highest gain while minimizing the noise figure and the amount of signal distortion/nonlinearities in the device.

The cliff for field testing at Dante's View is approximately 1780 m above the Death Valley floor. The antenna is positioned on the cliff to observe the moving Sun and track its direct path and reflection position on the valley floor. Due to the system's data volume limitations, the maximum acquisition time with the receiver's 15.36 MHz bandwidth is 8 s per measurement; after receiving each file, there is a data transfer time from the SDR to an external memory device that takes roughly 70 s. The effective PRF for the passive radar using this integration and transfer time is ≈ 0.012 Hz. For most of the test duration and Sun positions, this allows us to receive at most 5 files before the echo peak's delay time has moved the diameter of the Fresnel zone. We summarize the parameters for the Death Valley passive experiment in Table I.

C. End-to-End System Analysis

The gain of the cavity-backed bowtie antenna is roughly 6.5 dBi, the total external gain provided by the cascaded two front end LNAs is 44 dB, and the SDR's internal gain is 62 dB. Inside the SDR, the overall insertion loss from the antenna switch, SP3T switch, low pass filter, and RF transformer totals to -2.06 dB. Furthermore, the total SubMiniature version A (SMA) coaxial cable attenuation is estimated to be -2 dB. After considering these component losses, this gives a total of 108.44 dB RF gain. The expected front end signal power from to the Sun with a receiver bandwidth of 15.36 MHz is roughly -155 dBW [6], which gives a signal power of roughly -47 dBW at the analog-to-digital converter (ADC). As the ADC quantization noise is roughly -81 dB, our signal is over 30 dB greater than the quantization noise. Furthermore, the amplitude of the echo peak in the autocorrelation increases as $(T \cdot B_r)^{1/2}$ [6]; thus, the receiver's 8 s integration time and 15.36 MHz bandwidth produces autocorrelation peak gain of 40.45 dB. Using Death Valley roughness parameters from [49] to compute the roughness-induced reduction in the reflected power as in [50] and [5], the surface losses from the Death Valley desert floor reflection range from -8 dB to -22 dB.
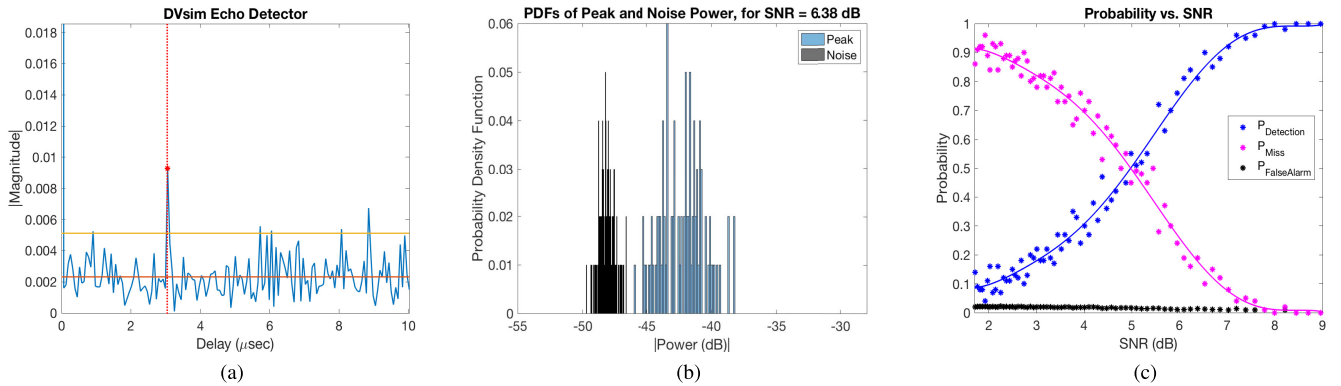
Fig. 3. Probability of detection metrics using (a) simulations of the Death Valley echo with expected link budget and Sun power level. The horizontal red and yellow lines in (a) correspond to the average noise power and the threshold for echo detection, respectively. (b) Example of the probability distribution for the autocorrelation's echo peak (blue bars) and its noise power (black), and (c) probability of detection curve as a function of SNR. The blue line in (c) corresponds to the probability of detection, and the magenta line to the probability of a missed event.

The 12 bit ADC in the SDR, therefore, has sufficient dynamic range to measure both the incoming direct signal and reflected signals without saturating the receiver. As the system's noise voltage is roughly an order of magnitude greater than the Sun's voltage, the 40.45 dB of coherent gain is sufficient to produce a distinct echo peak in the autocorrelation. Computing the SNR of the correlation's amplitude as in [6], and now including the anticipated Death Valley surface roughness losses, the passive radar's SNR for the Sun's echo therefore ranges from 2.4 to 16.4 dB.

D. Probability of Detection and Critical SNR

As found in Section III-C, the expected SNR for the Death Valley experiments can be less than 10 dB. Furthermore, we recognize the importance of transitioning from a deterministic measurement to a stochastic observation of the reflected signal, as we are sampling a Gaussian random process for each measurement [51]. We, therefore, analyze the radar's probability of detection vs. SNR, which is commonly done for active radar measurements [52]. Here, we simulate the Death Valley experiment 100 times for the expected range of SNR to create a probability of detection curve, as shown in Fig. 3(c). We automated the white noise echo detection process by choosing the largest autocorrelation echo peak above a threshold and within a reasonable time window of expected delays for that particular site, as shown in Fig. 3(a). While any variations in the solar spectrum from white noise could potentially manifest as sidelobes in Fig. 3(a), RFI filtering techniques in the signal processing chain can be used to remove disruptive sidelobe behavior in the autocorrelation [6], [53].

We found that we require an SNR of 4.98 dB to correctly detect the echo delay time greater than 50% of the time, and a critical SNR of at least 6.83 dB for a probability of detection greater than 90%. Similar to hypothesis testing for producing false alarm rates [52], we also provide the histograms of the autocorrelation's echo peak power and its noise power. In this simulation, the noise power is defined as the root-mean-square (rms) of the local noise floor in the autocorrelation function. As the SNR decreases, the probability distribution

functions (PDFs) begin to overlap, and false alarms are introduced, as shown in Fig. 3(b). In the high SNR regime, the histograms of the echo power and the noise power do not overlap at all, which is expected as a high SNR produces a high probability of detection.

E. Signal Processing Flow

The proposed signal processing approach is applied to the digitized complex signal, $x(n/f_s)$, where n is the sample number and f_s is the receiver's sampling rate, that is recorded by the SDR for T seconds. With $x(n/f_s)$ as its input, the aim is to generate a 2-D image that contains the surface reflection using the Sun as a radio source. The proposed approach is made up of four main steps: 1) signal segmentation, 2) RFI removal and autocorrelation, 3) echo peak extraction, and 4) 2-D image formation.

1) Signal Segmentation: Following the batches algorithm for passive radar [54], we take our received data and segment it into shorter sections. These segments decrease the effective pulse repetition interval (PRI) and are autocorrelated individually. The passive radar acquires a range line whenever it travels a distance $d = v \cdot PRI$ and forms the second dimension of the data matrix in the azimuth, or slow-time, direction. In addition to processing the data faster, segmenting the large data file into smaller lengths of $T_{seg} \leq T$ allows one to obtain subsequent measurements continuously. However, decreasing the integration time of each measurement effectively reduces the passive radar's SNR; thus, T_{seg} must be long enough for the correlation's echo peak to be above the noise floor.

2) RFI Removal and Autocorrelation: After segmenting the signal, we estimate its power spectral density (PSD) and remove any RFI in the frequency domain by amplitude thresholding the PSD to its 95th percentile [6]. To autocorrelate the signal, we then follow the Wiener-Khinchin theorem [51] by taking the inverse fast Fourier transform (FFT) of the PSD

$$C(\tau) = \mathcal{F}^{-1}\left\{ \frac{1}{T_{seg}} |X(f, T_{seg})|_A^2 \right\} \qquad (29)$$

where A denotes amplitude thresholding of the PSD, $X(f, T_{seg})$ is the T_{seg}-second length FFT of the segmented complex signal, x, and $\mathcal{F}^{-1}$ is the inverse FFT.

3) Echo Peak Extraction: After using our autocorrelation-based technique, we extract the amplitude and delay time of the echo peak in the autocorrelation. We additionally extract the phase of the echo peak. By monitoring the echo peak's phase, we are able to detect changes in the range that are less than the inherent range resolution, which is a function of the bandwidth [55]. Sampling this phase history is also necessary for passive SAR focusing.

4) 2-D Image Formation: After autocorrelating the signal, the obtained range lines for each measurement are then positioned side by side in range gate columns to form a 2-D range-compressed image, $C(\tau, u)$ [35]. We then take the FFT in the azimuth direction, u, to get the Range-Doppler image

$$I(\tau, \nu) = \mathcal{F}\{C(\tau, u)\} \tag{30}$$

where u denotes the slow time in the azimuth direction and ν is the Doppler frequency domain [54].

To summarize the signal processing, the key features are that we use the Sun as our signal of opportunity, the signal is received with one antenna, and the algorithm performs an autocorrelation via the Wiener–Khinchin theorem after removing RFI from the segmented signal. As the signal is received with one channel, we did not use direct signal suppression techniques, such as CLEAN, that rely on both a surveillance channel and reference channel for direct signal removal [56].

F. Measurement Diagnostics

We outline the key characteristics of the received signal and steps taken to perform diagnostics and error checking for each measurement. For all of the data presented in the experimental results, we observed that they were consistent with these diagnostics and signal statistics.

1) Time Domain Analysis: We first observe the time domain of the raw received signal to ensure that there is no clipping. We also estimate the average voltage waveform amplitudes and check that they are above the digitizer's noise level.

2) Frequency Domain Analysis: Second, we look at the PSD and spectrogram of the signal to ensure that there is no transient RFI in the observed spectrum. After going through the system, the Sun is assumed to be a band-limited white noise signal that is below the thermal noise floor. Therefore, we expect a broadband flat frequency spectrum that is free of man-made radio sources.

3) Received Signal Statistics: Next, we observe the statistics of the data, both in the time domain and the frequency domain. We expect the time domain voltage values to be Gaussian distributed. In the frequency domain, we expect the histogram of the received data's PSD to follow an exponential distribution. We also measure the signal's spectral kurtosis, which is equal to 3 for a white Gaussian noise (WGN) process [57].

4) Autocorrelation Characteristics: We then analyze the autocorrelation characteristics by ensuring that the observed echo peak's delay time and power match what we expect based on the Sun's angle, cliff height, desert floor slope, and surface

reflectivity from previous measurements of surface roughness parameters [49]. We also verify that the observed echo peak is not periodic, as periodic peaks correspond to autocorrelation ambiguities introduced by man-made radio sources.

5) Spatial Coherence and Pulse Broadening: Finally, we analyze the degradation of the spatial coherence of a source with the finite angular extent in terms of pulse broadening (i.e., delay smear in the autocorrelation) [3], as the Sun subtends a $\delta\theta = 0.6°$ angle in the sky [58], [59]. We estimate the pulse broadening, δt, due to the extended nature of the Sun by taking the difference in delay time, $\delta t = \Delta t(\theta - \delta\theta/2) - \Delta t(\theta + \delta\theta/2)$, where Δt is the echo delay time as a function of incidence angle, θ, and the angular size of the source, $\delta\theta$, [6]. For the receiver height and geometry of the experiment, we determined the pulse broadening produces a negligible delay spread that spans at most two samples, which is what we observe in the autocorrelation.

IV. RESULTS

The following results are divided into 3 subsections: 1) simulations of the passive Death Valley experiment with white Gaussian noise, 2) experimental field results of the passive testing at Death Valley, and 3) a 2-D full-wave simulation of passive SAR focusing using a white noise source.

A. Simulations of Sun's Reflection off Death Valley Floor

We first simulate the Death Valley experiment by generating a white noise echo that experiences scattering and reflection losses [60]. We use MATLAB's WGN function to simulate the white noise source at the power levels of the Sun's radio emissions by creating a vector of N white Gaussian noise samples in the time domain. We then FFT the simulated white noise to transform it to a frequency domain vector, $W(f)$, with length N. In the frequency domain, we create a copy of this white noise source vector and multiply it by a phase shift corresponding to the round-trip delay, $e^{-j2\pi fr/c}$. The delayed path of the white noise signal is then multiplied by a loss vector, ρ, that contains the reflection coefficient, a random phase vector between $\pm\pi/2$ to simulate scattering, and a scattering loss term (as described in Section II), before being added to the direct path signal. Finally, we create a separate WGN vector at the power levels of the thermal noise; after transforming the generated thermal noise to the frequency domain, $N(f)$, it is then added to the Sun's direct and reflected path. This process is summarized in the equation below

$$X_{sim}(f) = W(f) + \rho W(f)e^{-j2\pi fr/c} + N(f). \tag{31}$$

We then estimate the autocorrelation of the simulated echoed white noise, $X_{sim}(f)$, as described in 29. After obtaining the autocorrelation, we repeat this for an expected range of Sun angles to simulate the Sun moving in front of the cliff over the entire day. This simulated surface floor reflection of the Death Valley Experiment shows the Sun's echo as its elevation changes from 8° to 20°. The fast-time delay [Fig. 4(a)] maps to a surface height [Fig. 4(b)].
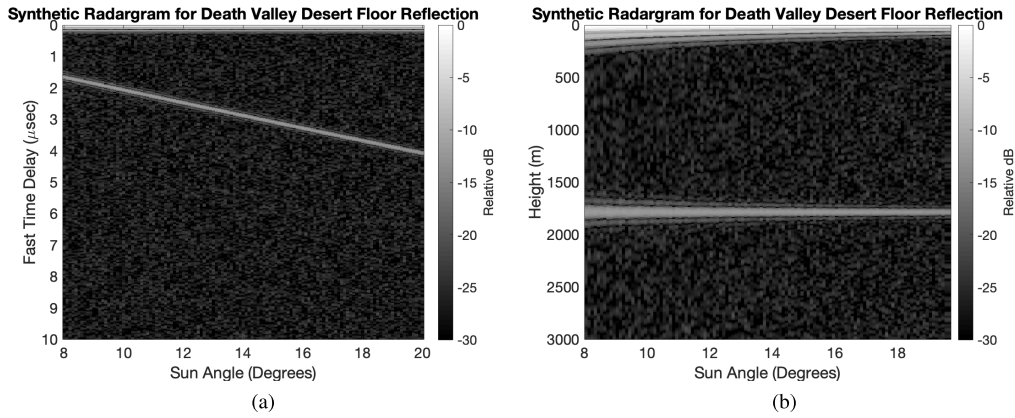
Fig. 4. Simulation of Death Valley Experiment as the Sun moves from 8° to 20°. The fast-time delay (a) of the Sun's isocurve reflection maps to a surface height (b). Note that the range resolution worsens as the Sun's elevation angle decreases, which is expected as the size of the Sun's reflection point increases.
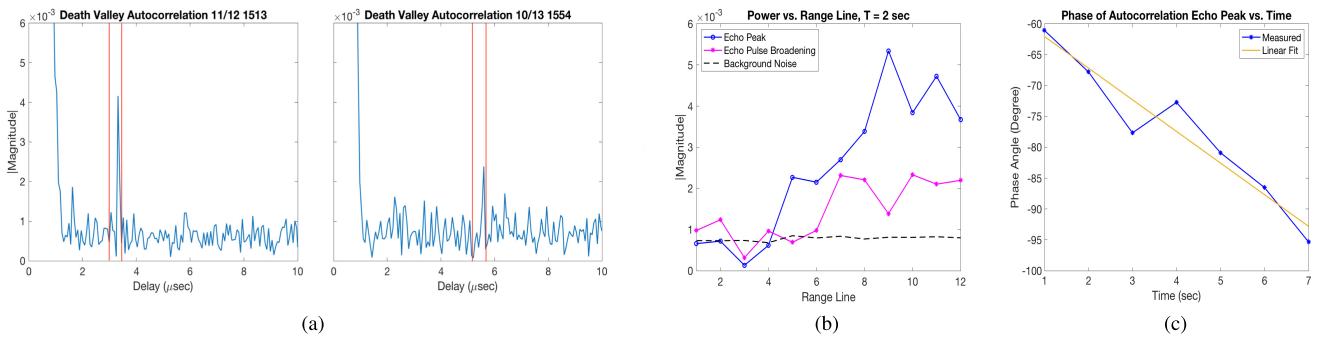

Fig. 5. Experimental results of the passive radar using the Sun to measure (a) changes in range that match the expected delay time (b) changes in reflected power and (c) changes in phase in the autocorrelation's echo peak over time. In (a), the vertical red lines correspond to the uncertainty in the expected delay time based on the estimated Sun's elevation angle (SunEarthTools), the height of the cliff (Google Earth), and the local slope of the desert floor (Shuttle Radar Topography Mission (SRTM) Death Valley DEM [61]). In (b), the blue line corresponds to the echo peak magnitude for each acquisition, and the black dashed line corresponds to the background noise in the autocorrelation; the magenta line corresponds to the magnitude of the echo pulse broadening, which we show is a subdominant effect.

B. Field Demonstration at Death Valley

With the described experimental setup in Section III-B, we demonstrate our passive technique's ability to extract the delay time, amplitude, and phase of the Sun's echo from the Death Valley floor.

1) Observed Changes in Range: We present two tests to highlight the change in the detected echo range as the Sun moves. The combination of the cliff height and the Sun angles at the time of these acquisitions (approximately 14.8° and 25.2°) predicts delay times that match the measured delay times of 3.32 and 5.60 ms, respectively [Fig. 5(a)]. The echo peak in the autocorrelation is within the estimated delay time, including the uncertainty (shown in red lines) in the Sun's elevation angle at the time of the measurement, the height of the cliff at the test site location using Google Earth, and the local slope of the desert floor obtained with a digital elevation model (DEM) [61] of the region—all of which have an impact on the expected delay time.

2) Observed Changes in Reflectivity: In addition to demonstrating that our passive technique can detect changes in range as the Sun's elevation angle changes with the time of day, we also demonstrate that our passive technique can detect changes in reflectivity [Fig. 5(b)]. Our observed changes in reflectivity [Fig. 5(b)] compares well with the Google Earth

DEM of the Death Valley desert floor, as the Sun's reflection point moved from a rougher region (with low surface reflectivity) to a smooth salt flat (with high surface reflectivity) [49].

We determined the expected changes in reflectivity by tracking the Sun's moving reflection point across the desert floor. Using the test site location, the height of the cliff, the time of the test period, and estimates of the Sun's elevation and azimuth positions, the reflection point's total movement during the test period was 273 m. In the range profile, we do not see a strong reflection for the first 8 s. There is then a delay of 70 s, where the Sun's reflection point moves 116 m. At the next received file, the echo power increases for the next 8 s. There is then another delay of 70 s, where the Sun's reflection point moves an additional 116 m. The power then slightly decreases for the final 8 s. We, therefore, attribute this change in observed power to changes in reflectivity, as a view of the surface features using Google Earth show that the Sun's reflection point was on rougher desert floor at the start of the test, began moving onto a salt flat of 210 m in length, and then moved completely onto it for the maximum reflectivity [Fig. 5(b)].

3) Observed Changes in Phase: Finally, we demonstrate that our passive technique can detect changes in the phase of the autocorrelation echo peak. For this demonstration,
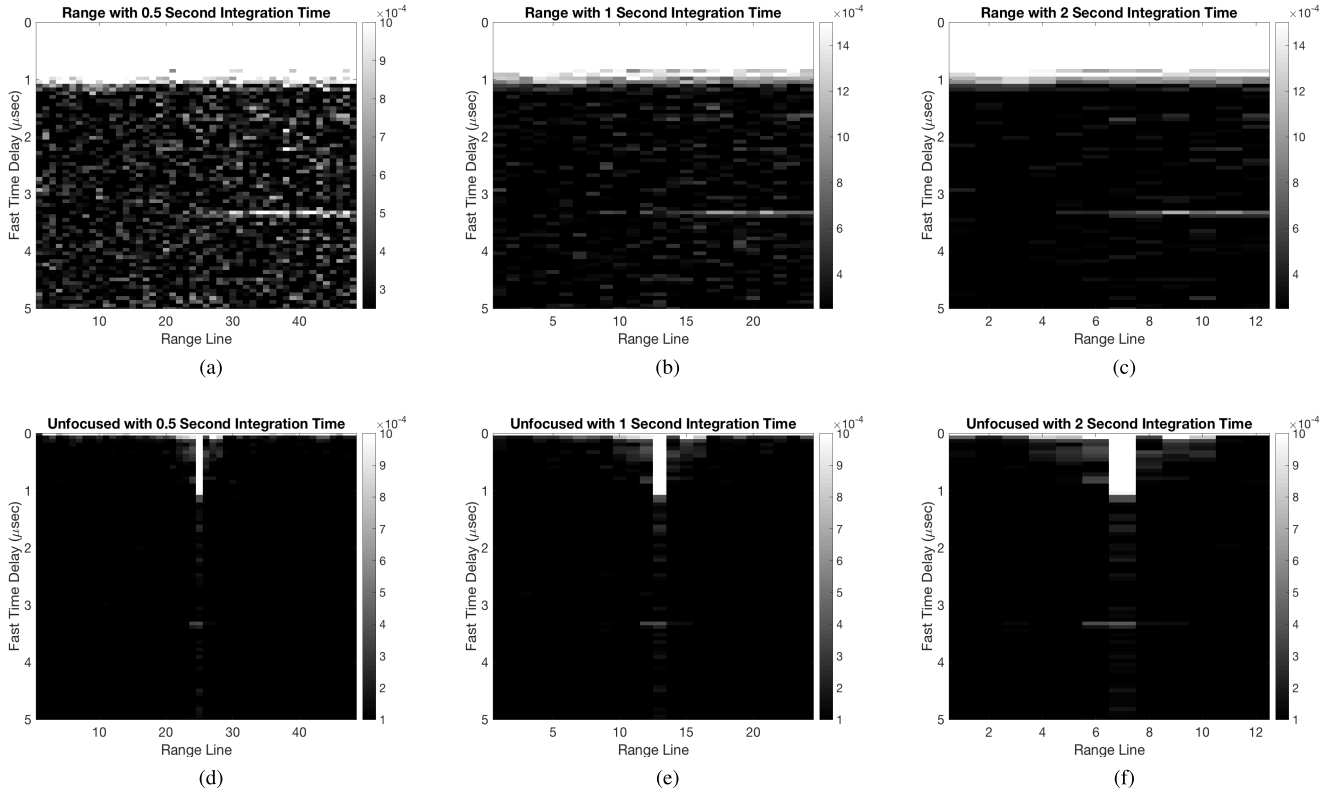
Fig. 6. Experimental results of the passive radar using the Sun with subset processing of three consecutive files to highlight the impact of integration time on the SNR and the change in reflected power over time. The top row (a)–(c) is the real aperture radar image, and the bottom row (d)–(f) is the unfocused image. The integration time increases from 0.5 s (a)–(d), 1 s (b)–(e), to 2 s (c)–(f) in the columns.

we segmented this 8 s file into 1 s intervals and autocorrelated each segment as described in III-E. We then extracted the phase of the echo peak from the autocorrelation. Fig. 5(c) shows the phase tracking using the 8 s file with the greatest SNR. We observe a linear change in phase over time, which we expect from the Sun's reflection point moving over this small time window and from 16, $\Delta\phi_D(t) = (2\pi/\lambda)\Delta r(t)$. This demonstrates that we can recover the phase history of the passive echo and that with a sufficient PRF, one could SAR focus the passive signal.

4) Unfocused SAR: We then align the autocorrelation measurements in range gate columns as described in Section III-E. The top row of Fig. 6 first shows this real aperture image after only range compression using increasing integration times from left to right of 0.5 s [Fig. 6(a)], 1 s [Fig. 6(b)], and 2 s [Fig. 6(c)]. We then take the FFT in the along track direction of an illuminated area the size of the Fresnel zone. The unfocused SAR result (Fig. 6, bottom row) shows the subset processing of three consecutive files using increasing integration times, T_{seg}, of duration 0.5 s [Fig. 6(d)], 1 s [Fig. 6(e)], and 2 s [Fig. 6(f)].

At 14.8°, and a cliff height of 1780 m, the range to the reflection point is $R = 6968$ m. Using a center frequency of 330 MHz, and aperture length $l = 1$ m, this gives a projected beam area $(R\lambda/l) = 6330$ m. The azimuth resolution for an unfocused acquisition is therefore $\delta_{az} = (\lambda R)^{1/2} = 79.6$ m. As the Sun's reflection point moves 273 m during our test period time, this corresponds to the

Sun moving roughly 3 azimuth samples in the 3 received files.

To determine the Doppler bandwidth of this received signal, we compute the Sun's reflection point velocity, v_s, by tracking the changes in its azimuth and elevation angle. At the time of our acquisition, the Sun's velocity was roughly 100 m/min. Between receiving each 8 s file, there is a 70 s time delay between taking each sample. This corresponds to the Sun's reflection point moving roughly 116 m during this period. In total, it took 164 s to receive the three presented 8 s data files. During this total time interval, the distance the Sun's reflection point moved is approximately 273 m. As the PRF of the passive radar is only 0.0128 Hz, this Doppler sampling is insufficient to recover the Doppler bandwidth of the Sun's reflection point when projected onto a linear aperture, which is $2 \cdot f_d = 4(v_s/\lambda) = 7.4$ Hz.

We, therefore, did not attempt azimuth focusing of the experimental data due to the insufficient passive PRF for Doppler sampling and the uneven timing between acquisitions. However, we observed changes in range, phase, and reflectivity, which are the necessary components to implement passive SAR. As such, we demonstrate Passive SAR focusing through simulations in Section IV-C.

C. Passive SAR Focusing Simulations

In this section, we present the results of our passive SAR simulations with synthetic data and compare them to those for an active SAR. This simulation considers a passive radar
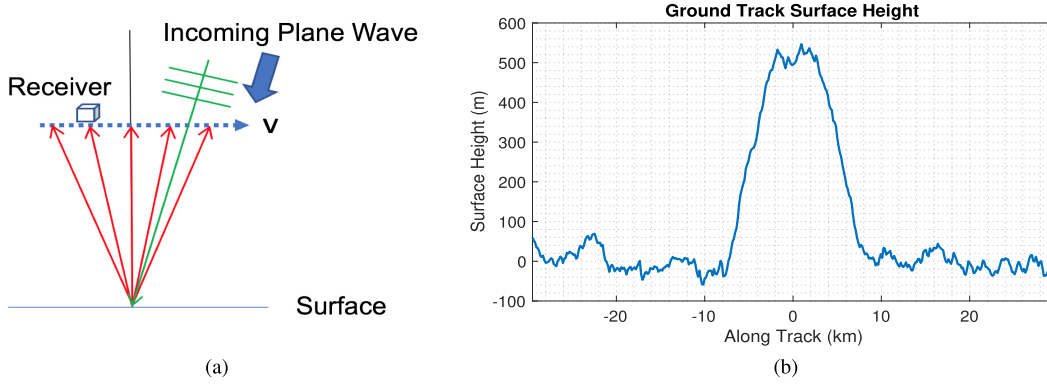
Fig. 7. (a) Sensor geometry for an incoming plane wave with a nonzero incidence angle. (b) DEM of the along-track profile for the active and passive SAR simulations.

onboard a platform that moves with constant velocity over a DEM as shown in Fig. 7. The sensor geometry for a passive instrument that receives the incoming plane waves is shown in Fig. 7(a), with the DEM of a ridge shown in Fig. 7(b).

In the case of the passive SAR simulations, the first receive window corresponds to receiving the direct incoming white noise plane wave of power P_d (1), as well as an extraneous signal that contains a previously reflected white noise plane wave of power P_r (2) and the background thermal noise. This first receive window is treated as the reference signal. The second receive window then contains the desired, reflected white noise plane wave of power P_r (2); however, this second window also contains additional noise with a new incoming direct white noise plane wave of power P_d (1), as well as new background thermal noise.

The voltage signals of the reference, V_{ref}, and reflected echo, V_r, are thus given by

$$V_{\text{ref}}(t) = \sqrt{P_d}s(t) + \sqrt{< |v(t)|^2 >}\gamma(t) + \sqrt{P_n}\gamma(t) \quad (32)$$
$$V_r(t) = \sqrt{P_d}\gamma(t) + v(t) + \sqrt{P_n}\gamma(t) \quad (33)$$

where $s(t)$ is the unit-amplitude incoming plane-wave white noise signal in the time domain, $v(t)$ is the simulated surface reflection based on $s(t)$ and P_r (2), $< |v(t)|^2 >$ is the average power of the reflected noise signals simulated in the absence of the direct signal and thermal noise, P_n is the thermal noise of the receiver, and $\gamma(t)$ is a draw from an independent complex standard normal distribution at each time sample t.

After correlating the received signals, we then perform azimuth focusing by using time-domain backprojection, as described in Section II. The time-domain signal is then normalized by the number of samples. Although there is no across-track processing, we note that the DEM is large enough to have point targets outside of the range window.

1) Parameters for the Active and Passive Simulations: The simulation parameters were chosen to highlight the application of this technique for the Radar for Icy Moon Exploration (RIME) [62] and the Radar for Europa Assessment and Sounding: Ocean to Near-Surface (REASON) [9], [63] instruments. The active and passive simulations share a center frequency of 9 MHz, bandwidth of 1 MHz, and PRF of 280.6 Hz. The radio source for the passive simulations is Jupiter's radio

TABLE II
SAR SIMULATION PARAMETERS

Description	Specification
Passive Signal Flux Density	10^{-14} W Hz^{-1} m^{-2}
Active Transmit Power	10 W
Center Frequency	9 MHz
Receiver Bandwidth	1 MHz
Passive Integration Time	100 μs
Active Chirp Length	20 μs
PRF	280.6 Hz
Sensor Velocity	4200 m/s
Sensor Altitude	25 km
Aperture Length	Fresnel Zone

emissions, which we model as a white noise source in the HF band [3], [64]. The integration time for the passive case is 100 μs, but could be greater to increase the passive SNR. The chirp length for the active case is 20 μs and is simulated as a range-compressed pulse with 1 MHz bandwidth, which corresponds to a 150 m range resolution. In this simulation, the sensor's velocity of 4200 m/s is for an orbital system at an altitude of 25 km. The power of the chirp signal is unity amplitude and a 10 W transmit power is applied. These system parameters are summarized in Table II.

2) Incident White Noise Plane Wave Generation and Acquisition: The passive and active cases have the same scene, sensor geometry, transmit pulse window, and receive window. For each simulation, a facet is treated as an isotropic radiator with radar cross section normalized to unity. Again, the radar equation for the active case [44] is $P_r = (P_t G_t G_r \lambda^2 \sigma / (4\pi)^3 R^4)$, while for the passive plane wave case [43] is $P_r = (SG_r \lambda^2 \sigma / (4\pi)^2 R^2)$.

To generate the white noise passive plane wave, we first define the integration time (pulselength) of the basebanded time-domain signal. We then define an oversampled baseband sample rate of $f_s = 50$ MHz. We next multiply the integration time by the baseband sample rate to compute the number of samples that will be received, and therefore the number of frequency points in the spectrum. This spectrum is initialized to zero for all frequencies within the band. After finding all frequency points within a rectangular window at ± 0.5 MHz, we give each sample a value drawn from a complex Gaussian
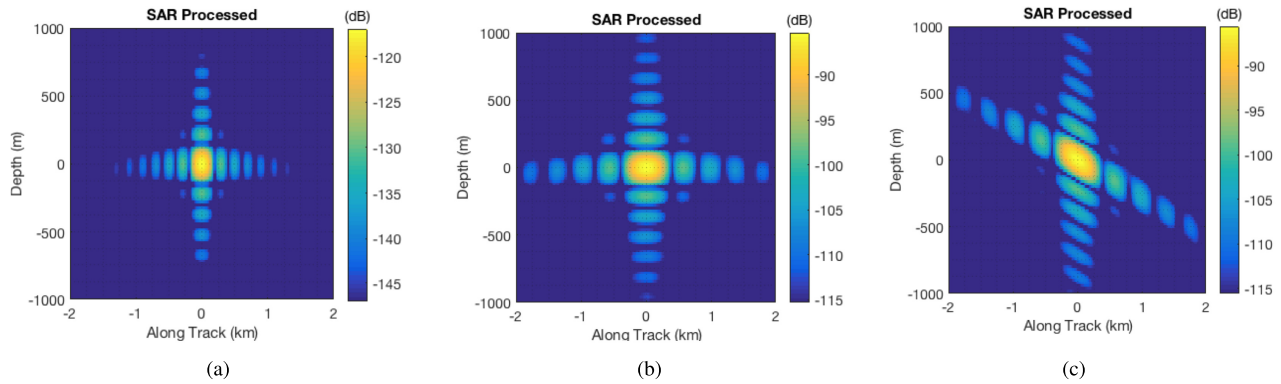
Fig. 8. Point scatter response for the Active and Passive systems. (a) Active SAR. (b) Passive SAR. (c) Passive SAR with 30° tilt in the incident plane wave. The along-track resolution for the passive case relative to the active degrades by a factor of 2 due to the one-way phase change.

distribution with unit amplitude. We then take the Inverse FFT to convert this signal back to the time domain.

3) Active Versus Passive Point Target Response: As noted in Section II-C, the slant range (one-way range delay) for active sounding is $\rho = r_1$, while the slant range for passive sounding is $\rho = (r_1 + r_2)/2$, where r_2 is the perpendicular distance from a target to a plane that is perpendicular to the planar wave's direction and centered at the middle of the sensor line. The phase for the active case is $e^{(i2kr_1)}$, while the phase for the passive case is $e^{(ik(r_1+r_2))}$.

Since r_2 is essentially a constant and only r_1 changes with sensor position, we observe a factor of 2 phase difference in the point-target response for the active [Fig. 8(a)] and passive [Fig. 8(b)]. Furthermore, the along-track resolution for the active and passive cases differ by a factor of two, which is supported by theory and simulation. This resolution difference is clearly observed between point target responses (a) and (b) of Fig. 8. We also note that when the plane wave for the passive case was incident at an angle 30° from normal along track, there is clearly visible tilt in the point scatter response that is 15° [Fig. 8(c)]. This tilt is expected as the bistatic side lobes are aligned perpendicular to the bisector of the source and receiver directions.

4) Active Versus Passive Range Compressed Result: Comparing the active and passive range compressed results, we see that the active system has a greater SNR and distinctly shows the geometry of the DEM [Fig. 9(a)]. Conversely, the SNR of the passive case where the incoming plane wave is a white noise signal, shows that with such a short integration time, the passive range compressed signal is barely detectable and does not clearly show the geometry of the tested DEM [Fig. 9(c)]. While these passive range-compressed and processed images are noisy, this is because the passive receive windows are not using the maximum compression gain. With an increase in integration time, the passive range-compressed image could recover the image, but at a greater data volume and computational expense.

5) Active Versus Passive SAR Focused Result: We then used SAR processing to focus the range compressed result for both the active and passive cases [Fig. 9(b) and (d)] using the backprojection algorithm described in Section II-E. The aperture length and image postings are equal to the Fresnel

zone radius for an altitude of 25 km, which is different between the active and passive; the active SAR azimuth resolution is $L_a = (\lambda h/2)^{1/2} = 645$ m [Fig. 9(b)], whereas the passive SAR azimuth resolution is $L_p = (\lambda h)^{1/2} = 912$ m [Fig. 9(d)]. Our simulations show that passive SAR focusing of a white noise signal is possible by monitoring the changes in range and phase and sampling the Doppler history. Although the active system has a greater SNR than the passive radar, the geometry of the DEM is clearly visible for both the active [Fig. 9(b)] and passive [Fig. 9(d)] cases.

In order to compare the SNR of the active and passive SAR focused images, we defined a transmit power for the active system, $P_t = 10$ W, and selected an incident power density for the passive case, $S = 10^{-14}$ W Hz^{-1} m^{-2}. This allowed us to relatively measure the difference between the passive and active cases. Furthermore, a meaningful comparison between the two techniques required that they used the same receiver front end (i.e., noise figure, thermal noise, and galactic background noise). While the active and passive sounding has a different SNR for the same target, the key takeaway of the results of our simulation is that a passive radar onboard a spacecraft can perform SAR focusing using a white noise signal to obtain an improvement in both SNR and azimuth resolution.

V. DISCUSSION

Our results show that even with such a short integration time, the SAR focused white noise signal can clearly recover the geometry of the tested DEM. Having demonstrated the potential for passive SAR focusing to improve the radar's SNR and azimuth resolution, we note that the passive SNR would further improve by using longer receiving windows, but at the cost of a greater data volume and computational expense for existing active sounders operating in a passive mode.

A system designed for passive sounding would therefore have several key differences to provide significant improvements to the performance described above. First, the data volume requirement would be significantly reduced if one used an field-programmable gate array (FPGA) to perform on-board processing of the data in real-time and stored the final processed result [6]. This would enable the use of the maximum passive SAR focusing integration time of
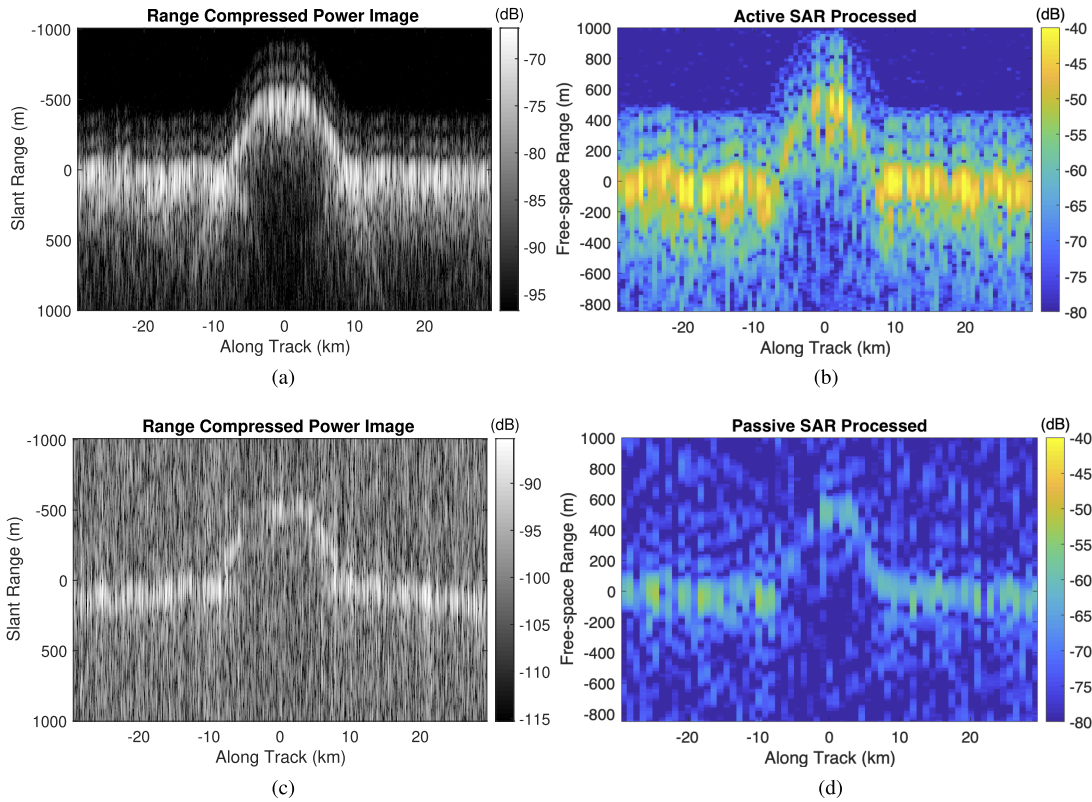
Fig. 9. Range Compressed and SAR Simulations for Active and Passive Systems. (Top) Active (a) range-compressed and (b) SAR focused results. (Bottom) Passive (c) range-compressed and (d) SAR focused results. The results of our simulations with synthetic data show that passive SAR focusing can be used to increase the SNR and improve the azimuth resolution of acquisitions made with a white noise signal.

$T_{\max,D} = \lambda/(4v) = 1984$ μs (instead of the 100 μs receive window used in the simulation) and would increase the SNR of the passive radar by 13 dB (23, assuming the same aperture size as in the simulation). Thus, by using the full integration time, the maximum theoretical SNR for the passive system would be comparable to the active system's SNR. Furthermore, a passive sounder can be sensitive to greater bandwidths by using an electrically short antenna [3]. While increasing the bandwidth would improve the range resolution and suppress the main lobe and side lobes in the autocorrelation, this factor would not improve the SNR for a distant target, which is also shown in 23. Further improvements in SNR could be obtained by increasing the size of the synthetic aperture; where again we note that the length of $T_{\max,ap}$ in 23 can be limited by 1) the Fresnel zone in the case of a flat, coherent reflector [44], 2) the length of the radar's receive window when focusing onto a single isotropic scatterer [47], or 3) the surface's scattering function, which is the scope of a follow-on study. While the active SAR azimuth resolution would still be better by a factor of $\sqrt{2}$, even for an optimized passive system design, the optimized passive performance would be comparable to active sounding.

Another improvement to passive sounding would be the use of direct signal suppression. While direct signal interference (DSI) mitigation techniques are commonly used for passive radar [56], existing algorithms rely on both a surveillance channel and a reference channel for DSI removal, whereas this

experiment was performed using only one receive antenna. DSI suppression with a single channel will be the subject of a follow-on article, as it is unexplored in the context of receiving white noise sources, such as the Sun.

Lastly, a potentially limiting factor for the passive sounding technique is the extent of spatial coherence for both the Sun and Jupiter's radio emissions. We considered the spatial decoherence of the source in terms of pulse broadening, which depends on the angular size of the source (where $\delta\theta_S = 0.6°$ for the Sun at Earth [58], [59], and $\delta\theta_J \leq 0.034°$ for Jupiter's radio emissions at Europa [3]), the incidence angle, the platform height of the receiver, and the path length difference between the direct and reflected signals [6]. Although we determined the pulse broadening to be a subdominant effect for our experiment, the delay smear of the Sun's echo in the autocorrelation can become an issue for large incidence angles and platform heights. We show the expected pulse broadening of the Sun's echo [(11) in [6]] as a function of platform height and incidence angle for our 15 MHz receiver (Fig. 10). While the pulse broadening becomes much greater than the pulsewidth for a 15 MHz receiver as the platform height and incidence angle increases, the pulse broadening is not an issue for small incidence angles, even for large platform altitudes greater than 500 km.

While the coherence limitation requirement using the Sun is met for terrestrial ground-based experiments with small antenna altitudes and large incidence angles, this factor could
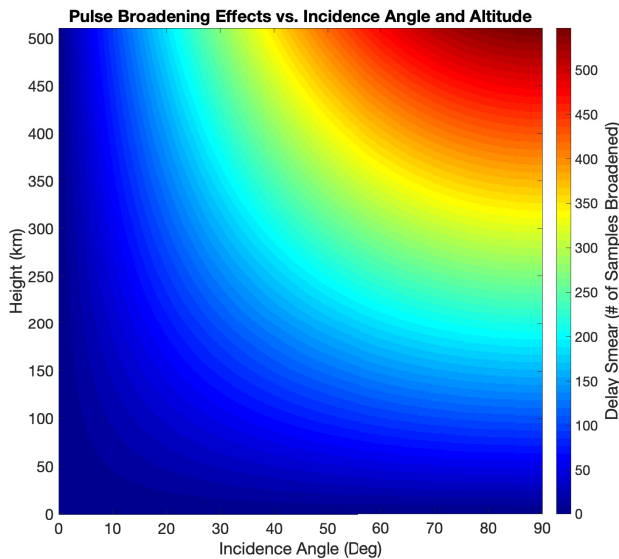
Pulse Broadening Effects vs. Incidence Angle and Altitude

Fig. 10. Pulse broadening effects using the Sun with angular size of $\delta\theta = 0.6°$. As the platform height and incidence angle increases, the pulse broadening becomes much greater than the pulsewidth for a 15 MHz receiver, and the delay smear of the echo peak can spread over hundreds of samples in the autocorrelation function.

present an issue for spacecraft with much higher platform altitudes than terrestrial ground-based receivers. As the Sun is an extended source, the extent to which the spatial coherence of the Sun limits spacecraft measurements to small incidence angles or near-zenith positions will be the subject of a follow-on study.

VI. Conclusion

In this article, we presented our passive radio sounding approach's ability to perform SAR focusing using a white noise signal. We found that our passive sounding experimental prototype was able to observe changes in the range, phase, and reflectivity of the Sun's echo over time as it received reflections from a rougher surface, which demonstrate the fundamental capability of the passive system to sample the delay and Doppler information required for SAR processing using the Sun. In addition to performing 2-D imaging of the desert floor, we also determined a critical SNR of 6.83 dB for a probability of detection of at least 0.9; this will be crucial for future testing and deployments with our passive system to monitor ice sheets at a larger scale with high fidelity results.

With our unfocused experimental result on a short acquisition as a first step, future improvements to our system include managing the phase history between subsequent measurements, using longer acquisition times with higher sampling rates, and combining a day's worth of range lines to form a larger 2-D image. An *in situ* demonstration of passive SAR will also require more accurate timing of acquisitions as well as tracking of the Sun's changing elevation and azimuth position in order to focus the received data.

Finally, our simulations of passive SAR demonstrate that one can focus a white noise signal to improve the azimuth resolution and SNR of passive radio sounding measurements.

Developing this method's measurement capabilities is crucial to ultimately monitor ice sheets with passive radars that would not only complement active systems but offer resource efficiencies that could enable deployments that perform on larger spatial scales and with higher temporal resolution. Once miniaturized and deployed for an extended period of time, a passive receiver could map the topography and geometry of the ice sheet bed as the Sun moves throughout the entire day and perform repeat measurements over a 24-h period. By using the Sun or Jupiter as the source for echo detection, such a passive SAR technique would serve as a low-resource approach for both planetary sounding and subsurface imaging.

References

[1] V. U. Zavorotny, S. Gleason, E. Cardellach, and A. Camps, "Tutorial on remote sensing using GNSS bistatic radar of opportunity," *IEEE Geosci. Remote Sens. Mag.*, vol. 2, no. 4, pp. 8–45, Dec. 2014.

[2] H. Griffiths and C. Baker, *An Introduction to Passive Radar*, 1st ed. Boston, MA, USA: Artech House, 2017.

[3] A. Romero-Wolf, S. Vance, F. Maiwald, E. Heggy, P. Ries, and K. Liewer, "A passive probe for subsurface oceans and liquid water in Jupiter's icy moons," *Icarus*, vol. 248, pp. 463–477, Mar. 2015, doi: 10.1016/j.icarus.2014.10.043.

[4] A. Romero-Wolf *et al.*, "Prospects of passive radio detection of a subsurface ocean on Europa with a lander," *Planet. Space Sci.*, vol. 129, pp. 118–121, Sep. 2016, doi: 10.1016/j.pss.2016.06.010.

[5] D. M. Schroeder *et al.*, "Assessing the potential for passive radio sounding of Europa and Ganymede with RIME and REASON," *Planet. Space Sci.*, vol. 134, pp. 52–60, Dec. 2016, doi: 10.1016/j.pss.2016.10.007.

[6] S. T. Peters, D. M. Schroeder, D. Castelletti, M. Haynes, and A. Romero-Wolf, "*In Situ* demonstration of a passive radio sounding approach using the sun for echo detection," *IEEE Trans. Geosci. Remote Sens.*, vol. 56, no. 12, pp. 7338–7349, Dec. 2018.

[7] V. Bogorodskii, C. Bentley, and P. Gudmandsen, *Radioglaciology*, 1st ed. Dordrecht, The Netherlands: D. Reidel, 1983.

[8] D. M. Schroeder *et al.*, "Five decades of radioglaciology," *Ann. Glaciol.*, vol. 61, no. 81, pp. 1–13, Apr. 2020.

[9] D. Blankenship, D. Young, W. Moore, and J. C. Moore, "Radar sounding of Europa's subsurface properties and processes: The view from Earth," in *Proc. Europa*, Sep. 2009, pp. 631–653.

[10] L. Bruzzone, G. Alberti, C. Catallo, A. Ferro, W. Kofman, and R. Orosei, "Subsurface radar sounding of the Jovian moon Ganymede," *Proc. IEEE*, vol. 99, no. 5, pp. 837–857, May 2011.

[11] W. Chu, D. M. Schroeder, H. Seroussi, T. T. Creyts, and R. E. Bell, "Complex basal thermal transition near the onset of Petermann Glacier, Greenland," *J. Geophys. Res., Earth Surf.*, vol. 123, no. 5, pp. 985–995, May 2018.

[12] A. K. Kendrick *et al.*, "Surface meltwater impounded by seasonal englacial storage in West Greenland," *Geophys. Res. Lett.*, vol. 45, no. 19, pp. 1–8, Oct. 2018.

[13] J. A. Dowdeswell and S. Evans, "Investigations of the form and flow of ice sheets and glaciers using radio-echo sounding," *Rep. Prog. Phys.*, vol. 67, no. 10, pp. 1821–1861, Oct. 2004.

[14] G. A. Catania, T. A. Scambos, H. Conway, and C. F. Raymond, "Sequential stagnation of Kamb ice stream, West Antarctica," *Geophys. Res. Lett.*, vol. 33, no. 14, pp. 2–5, 2006.

[15] J. Mouginot, E. Rignot, and B. Scheuchl, "Sustained increase in ice discharge from the Amundsen Sea Embayment, West Antarctica, from 1973 to 2013," *Geophys. Res. Lett.*, vol. 41, no. 5, pp. 1576–1584, Mar. 2014.

[16] T. Moon *et al.*, "Distinct patterns of seasonal Greenland glacier velocity," *Geophys. Res. Lett.*, vol. 41, no. 20, pp. 7209–7216, Oct. 2014.

[17] G. H. Gudmundsson, "Fortnightly variations in the flow velocity of Rutford ice stream, West Antarctica," *Nature*, vol. 444, no. 7122, pp. 1063–1064, Dec. 2006.

[18] M. R. Siegfried, H. A. Fricker, S. P. Carter, and S. Tulaczyk, "Episodic ice velocity fluctuations triggered by a subglacial flood in West Antarctica," *Geophys. Res. Lett.*, vol. 43, no. 6, pp. 2640–2648, Mar. 2016.

[19] S. T. Peters, D. M. Schroeder, D. Castelletti, M. Haynes, and A. Romero-Wolf, "First *in-situ* demonstration of passive radio sounding using the sun as a source for echo detection," in *Proc. IEEE Int. Geosci. Remote Sens. Symp. (IGARSS)*, Jul. 2018, pp. 4154–4157.

[20] S. T. Peters, D. M. Schroeder, D. Castelletti, M. S. Haynes, and A. Romero-Wolf, "Two dimensional image formation with passive radar using the sun for echo detection," in *Proc. IEEE Int. Geosci. Remote Sens. Symp. (IGARSS)*, Yokohama, Japan, Jul. 2019, pp. 10091–10094.

[21] A. Moreira, P. Prats-Iraola, M. Younis, G. Krieger, I. Hajnsek, and K. P. Papathanassiou, "A tutorial on synthetic aperture radar," *IEEE Geosci. Remote Sens. Mag.*, vol. 1, no. 1, pp. 6–43, Mar. 2013.

[22] C. Leuschen, S. Gogineni, and D. Tammana, "SAR processing of radar echo sounder data," in *Proc. Int. Geosci. Remote Sens. Symp. (IGARSS)*, vol. 6, Jul. 2000, pp. 2570–2572.

[23] J. J. Legarsky, S. P. Gogineni, and T. L. Akins, "Focused synthetic aperture radar processing of ice-sounder data collected over the Greenland ice sheet," *IEEE Trans. Geosci. Remote Sens.*, vol. 39, no. 10, pp. 2109–2117, Oct. 2001.

[24] D. A. Braaten, S. P. Gogineni, D. Tammana, S. Namburi, J. Paden, and K. K. Gurumoorthy, "Improvement of radar ice-thickness measurements of Greenland outlet glaciers using SAR processing," *Ann. Glaciol.*, vol. 35, pp. 73–78, 2002, doi: 10.3189/172756402781816852.

[25] M. E. Peters, D. D. Blankenship, S. P. Carter, S. D. Kempf, D. A. Young, and J. W. Holt, "Along-track focusing of airborne radar sounding data from West Antarctica for improving basal reflection analysis and layer detection," *IEEE Trans. Geosci. Remote Sens.*, vol. 45, no. 9, pp. 2725–2736, Sep. 2007.

[26] F. Heliere, C.-C. Lin, H. Corr, and D. Vaughan, "Radio echo sounding of Pine Island Glacier, West Antarctica: Aperture synthesis processing and analysis of feasibility from space," *IEEE Trans. Geosci. Remote Sens.*, vol. 45, no. 8, pp. 2573–2582, Aug. 2007.

[27] M. Soumekh, *Synthetic Aperture Radar Signal Processing With MATLAB Algorithms*. Hoboken, NJ, USA: Wiley, 1999.

[28] A. F. Yegulalp, "Fast backprojection algorithm for synthetic aperture radar," in *Proc. IEEE Radar Conf. Radar Next Millennium*, Apr. 1999, pp. 60–65.

[29] Y. Ding and D. C. J. Munson, "A fast back-projection algorithm for bistatic SAR imaging," in *Proc. Int. Conf. Image Process.*, Rochester, NY, USA, Sep. 2002, pp. 449–452.

[30] L. M. H. Ulander, H. Hellsten, and G. Stenstrom, "Synthetic-aperture radar processing using fast factorized back-projection," *IEEE Trans. Aerosp. Electron. Syst.*, vol. 39, no. 3, pp. 760–776, Jul. 2003.

[31] O. Frey, E. H. Meier, and D. R. Nüesch, "Processing SAR data of rugged terrain by time-domain back-projection," *Proc. SPIE*, vol. 5980, pp. 71–79, Oct. 2005, doi: 10.1117/12.627647.

[32] A. Kusk and J. Dall, "SAR focusing of P-band ice sounding data using back-projection," in *Proc. IEEE Int. Geosci. Remote Sens. Symp.*, Jul. 2010, pp. 4071–4074. [Online]. Available: https://ieeexplore.ieee.org/document/5651038

[33] M. I. Duersch, "Backprojection for synthetic aperture radar," Ph.D. dissertation, Dept. Elect. Comput. Eng., Brigham Young Univ., Provo, UT, USA, Jun. 2013.

[34] R. Bamler, "A comparison of range-Doppler and wavenumber domain SAR focusing algorithms," *IEEE Trans. Geosci. Remote Sens.*, vol. 30, no. 4, pp. 706–713, Jul. 1992.

[35] I. G. Cumming and F. H. Wong, *Digital Processing of Synthetic Aperture Radar Data: Algorithms and Implementation*. Norwood, MA, USA: Artech House, 2005.

[36] C. Prati, F. Rocca, D. Giancola, and A. M. Guarnieri, "Passive geosynchronous SAR system reusing backscattered digital audio broadcasting signals," *IEEE Trans. Geosci. Remote Sens.*, vol. 36, no. 6, pp. 1973–1976, Nov. 1998.

[37] M. Cherniakov, E. Plakidis, M. Antoniou, and R. Zuo, "Passive space-surface bistatic SAR for local area monitoring: Primary feasibility study," in *Proc. Eur. Radar Conf. (EuRAD)*, Rome, Italy, Oct. 2009, pp. 89–92. [Online]. Available: https://ieeexplore.ieee.org/document/5307044

[38] M. Antoniou, Z. Zeng, L. Feifeng, and M. Cherniakov, "Experimental demonstration of passive BSAR imaging using navigation satellites and a fixed receiver," *IEEE Geosci. Remote Sens. Lett.*, vol. 9, no. 3, pp. 477–481, May 2012.

[39] P. Samczynski and K. Kulpa, "Passive SAR imaging using a satellite pulsed radar as an illuminator of opportunity," in *Proc. 13th Int. Radar Symp.*, May 2012, pp. 157–161.

[40] B. Yonel, E. Mason, and B. Yazici, "Deep learning for passive synthetic aperture radar," *IEEE J. Sel. Topics Signal Process.*, vol. 12, no. 1, pp. 90–103, Feb. 2018.

[41] K. W. Nicholls, H. F. Corr, C. L. Stewart, L. B. Lok, P. V. Brennan, and D. G. Vaughan, "A ground-based radar for measuring vertical strain rates and time-varying basal melt rates in ice sheets and shelves," *J. Glaciol.*, vol. 61, no. 230, pp. 1079–1087, 2015.

[42] R. Drews *et al.*, "Actively evolving subglacial conduits and eskers initiate ice shelf channels at an Antarctic grounding line," *Nature Commun.*, vol. 8, no. 1, pp. 1–10, Aug. 2017.

[43] M. S. Haynes, "Surface and subsurface radar equations for radar sounders," *Ann. Glaciol.*, vol. 61, no. 81, pp. 135–142, Apr. 2020, doi: 10.1017/aog.2020.16.

[44] M. S. Haynes, E. Chapin, and D. M. Schroeder, "Geometric power fall-off in radar sounding," *IEEE Trans. Geosci. Remote Sens.*, vol. 56, no. 11, pp. 6571–6585, Nov. 2018.

[45] F. Ulaby *et al.*, *Microwave Radar and Radiometric Remote Sensing*. Ann Arbor, MI, USA: The Univ. of Michigan Press, 2014.

[46] A. Doerry, "Performance limits for synthetic aperture radar—Second edition," Sandia Nat. Lab., Albuquerque, NM, USA, Tech. Rep. 02, 2006.

[47] D. M. Schroeder, D. Castelletti, and I. Pena, "Revisting the limits of azimuth processing gain for radar sounding," in *Proc. IEEE Int. Geosci. Remote Sens. Symp. (IGARSS)*, Jul. 2019, pp. 994–996.

[48] C. Gerekos, L. Bruzzone, and M. Imai, "A coherent method for simulating active and passive radar sounding of the Jovian icy moons," *IEEE Trans. Geosci. Remote Sens.*, vol. 58, no. 4, pp. 1–16, Apr. 2019.

[49] M. K. Shepard, B. A. Campbell, M. H. Bulmer, T. G. Farr, L. R. Gaddis, and J. J. Plaut, "The roughness of natural terrain: A planetary and remote sensing perspective," *J. Geophys. Res. E, Planets*, vol. 106, no. E12, pp. 32777–32795, 2001.

[50] M. E. Peters, "Analysis techniques for coherent airborne radar sounding: Application to West Antarctic ice streams," *J. Geophys. Res.*, vol. 110, no. B6, pp. 1–17, Jun. 2005.

[51] J. S. Bendat and A. G. Piersol, *Random Data: Analysis and Measurement Procedures*, 4th ed. Hoboken, NJ, USA: Wiley, 2010.

[52] B. Mahafza, *Radar Signal Analysis and Processing Using MATLAB*. Boca Raton, FL, USA: Taylor & Francis, 2009.

[53] P. A. Fridman and W. A. Baan, "RFI mitigation methods in radio astronomy," *Astron. Astrophys.*, vol. 378, no. 1, pp. 327–344, 2001.

[54] C. Moscardini, D. Petri, A. Capria, M. Conti, M. Martorella, and F. Berizzi, "Batches algorithm for passive radar: A theoretical analysis," *IEEE Trans. Aerosp. Electron. Syst.*, vol. 51, no. 2, pp. 1475–1487, Apr. 2015.

[55] P. V. Brennan, K. Nicholls, L. B. Lok, and H. Corr, "Phase-sensitive FMCW radar system for high-precision Antarctic ice shelf profile monitoring," *IET Radar, Sonar Navigat.*, vol. 8, no. 7, pp. 776–786, Aug. 2014.

[56] J. L. Garry, C. J. Baker, and G. E. Smith, "Evaluation of direct signal suppression for passive radar," *IEEE Trans. Geosci. Remote Sens.*, vol. 55, no. 7, pp. 3786–3799, Jul. 2017.

[57] R. Dwyer, "Detection of non-Gaussian signals by frequency domain kurtosis estimation," in *Proc. IEEE Int. Conf. Acoust., Speech, Signal Process. (ICASSP)*, Apr. 1993, pp. 607–610.

[58] G. Swarup, V. K. Kapahi, J. D. Isloor, and R. P. Sinha, "Radio observations of the quiet sun at 49 cm," *Nature*, vol. 212, no. 5065, pp. 910–911, Nov. 1966.

[59] C. Vocks *et al.*, "LOFAR observations of the quiet solar corona," *Astron. Astrophys.*, vol. 614, no. 30067, pp. 1–10, 2018.

[60] S. T. Peters, D. M. Schroeder, and A. Romero-Wolf, "Passive radio sounding to correct for Europa's ionospheric distortion of VHF signals," *Planet. Space Sci.*, vol. 187, Aug. 2020, Art. no. 104925.

[61] E. Rodríguez, C. S. Morris, and J. E. Belz, "A global assessment of the SRTM performance," *Photogramm. Eng. Remote Sens.*, vol. 72, no. 3, pp. 249–260, Mar. 2006.

[62] L. Bruzzone *et al.*, "RIME: Radar for icy moon exploration," in *Proc. IEEE Int. Geosci. Remote Sens. Symp. (IGARSS)*, Jul. 2013, pp. 3907–3910.

[63] C. Grima, D. D. Blankenship, and D. M. Schroeder, "Radar signal propagation through the ionosphere of Europa," *Planet. Space Sci.*, vol. 117, pp. 421–428, Nov. 2015.

[64] B. Cecconi *et al.*, "Natural radio emission of Jupiter as interferences for radar investigations of the icy satellites of Jupiter," *Planet. Space Sci.*, vol. 61, no. 1, pp. 32–45, Feb. 2012.

Sean T. Peters (Member, IEEE) received the B.Sc. degree (*cum laude*) in electrical engineering from Rice University, Houston, TX, USA, in 2015, and the M.Sc. degree in electrical engineering from Stanford University, Stanford, CA, USA, in 2017, where he is pursuing the Ph.D. degree in electrical engineering with the Department of Geophysics and Electrical Engineering under the supervision of Assistant Professor D. Schroeder.

As a part of the Radio Glaciology Research Group, he was involved in developing ambient noise radio glaciology with the Radar Systems Development Team, Stanford University.

Mr. Peters received the National Science Foundation Graduate Research Fellowship, the Stanford's Diversifying Academia Recruiting Excellence Doctoral Fellowship, the Stanford Enhancing Diversity in Graduate Education-Science, Technology, Engineering, and Mathematics Fellowship, and Stanford Engineering's Larry and Joan Owen Fellowship.

Dustin M. Schroeder (Senior Member, IEEE) received the B.A. degree in physics and the B.S.E.E. degree (*magna cum laude*) in electrical engineering from Bucknell University, Lewisburg, PA, USA, in 2007, and the Ph.D. degree in geophysics from The University of Texas at Austin, Austin, TX, USA, in 2014.

He is an Assistant Professor of geophysics and (by courtesy) of electrical engineering with Stanford University, Stanford, CA, USA. He is also a Faculty Member with the Stanford Woods Institute for the Environment, Stanford. His research group seeks to approach problems from both an earth system science and radar system engineering perspective. He is a Science Team Member on the Radar for Europa Assessment and Sounding: Ocean to Near-Surface (REASON) Instrument on NASA's Europa Clipper Mission and the Mini-RF Instrument on NASA's Lunar Reconnaissance Orbiter. He has participated in three Antarctic field seasons with the Investigating the Cryospheric Evolution of the Central Antarctic Plate (ICECAP) Project and NASA's Operation Ice Bridge, as a Radar Engineer and an Operator. His research interests include observing and understanding the role that subglacial water plays in the evolution and stability of continental ice sheets and its contribution to the rate of sea level rise, and also include the development, use, and analysis of geophysical radar remote sensing systems that are optimized to observe hypothesis-specific phenomena.

Mark S. Haynes (Member, IEEE) received the B.S.E.-E.E. and B.M.A. (cello), and the M.S.E.-E.E. and Ph.D. degrees in applied physics from the University of Michigan, Ann Arbor, MI, USA, in 2006, 2011, and 2012, respectively.

From 2012 to 2013, he was a Post-Doctoral Research Associate with the Department of Electrical Engineering, University of Southern California at Los Angeles, Los Angeles, CA, USA. Since, he has been with the Radar Science and Engineering Section, Jet Propulsion Laboratory, National Aeronautics and Space Administration, Pasadena, CA, USA, where he has been involved in the Surface Water and Ocean Topography (SWOT) mission, AirSWOT, and REASON instruments and missions.

Dr. Haynes was a recipient of the Pre-Doctoral Traineeship Fellowship at the Department of Defense, the Breast Cancer Research Program, in 2008, and the NASA Honor Award Early Career Public Achievement Medal in 2018.

Davide Castelletti (Member, IEEE) received the Laurea (B.S.) and Laurea Specialistica (M.S.) degrees in telecommunication engineering and the Ph.D. degree in information and communication technologies from the University of Trento, Trento, Italy, in 2009, 2012, and 2017, respectively.

He was part of the team at the University of Trento, where he was involved in the design of the Radar for Icy Moon Exploration instrument for the Jupiter Icy Moons Explorer Mission of the European Space Agency. In 2014, he joined the Jet Propulsion Laboratory, Pasadena, CA, USA, as a Visiting Ph.D. Student, where he was involved in the clutter discrimination using an interferometric two-channel very high-frequency radar sounder. As a former Post-Doctoral Scholar at Stanford University, he worked with Assistant Professor D. Schroeder on problems in radar sounder interferometry and radar system engineering. His research interests include remote sensing, signal processing, and radar sounder instruments design.

Andrew Romero-Wolf received the B.A. degree in mathematics, the B.A. degree (Hons.) in physics from the University of Chicago, Chicago, IL, USA, in 2002, the master's degree in physical science from the University of Chicago in 2005, and the Ph.D. degree from the University of Hawaii at Manoa, Honolulu, HI, USA, in 2010.

He is a member of the Technical Staff with the Deep Space Tracking Group, Jet Propulsion Laboratory, California Institute of Technology, Pasadena, CA, USA. He has also served as the Investigation Scientist for the Radar for Europa Assessment and Sounding: Ocean to Near-surface instrument on NASA's Europa Clipper Mission. He has participated in NASA's Transition Radiation Array for Cosmic Energetic Radiation and Antarctic Impulsive Transient Antenna scientific ballooning experiments. His research interests include the radio detection of ultrahigh energy neutrinos, radio astronomy, direct imaging of exoplanets, and the development of passive sounding using radio astronomical sources.